Research Square

Preprints are preliminary reports that have not undergone peer review.
They should not be considered conclusive, used to inform clinical practice,
or referenced by the media as validated information.

Microglial HIF-1α-Driven Lactate Reprogramming Disrupts Cancer Metabolism and Redox Homeostasis in Glioma via TTF

Pengjie Hong

hpj_huashan@163.com

Fudan University Huashan Hospital Department of Neurosurgery https://orcid.org/0009-0007-9689-0026

Xianxin Qiu

Huashan Hospital Fudan University

Wanzun Lin

Ruijin Hospital: Shanghai Jiao Tong University Medical School Affiliated Ruijin Hospital

Huiling Fang

Chinese Academy of Sciences Key Laboratory of RNA Biology

Zhengjin He

Chinese Academy of Sciences Shanghai Branch

Mingxian Liu

Chinese Academy of Sciences Key Laboratory of RNA Biology

Kezhu Chen

Radboudumc Department of Neurosurgery

Tianwen Li

Fudan University Huashan Hospital Department of Neurosurgery

Junjie Zhong

Fudan University Huashan Hospital Department of Neurosurgery

Tongming Zhu

Fudan University Huashan Hospital Department of Neurosurgery

Qisheng Tang

Fudan University Huashan Hospital Department of Neurosurgery

Chencheng Ma

Huashan Hospital Fudan University

Zhiguang Pan

Fudan University Huashan Hospital Department of Neurosurgery

jianhong Zhu

Fudan University Huashan Hospital Department of Neurosurgery

Yang Wang
Huashan Hospital Fudan University
Hai Jiang
Chinese Academy of Sciences Key Laboratory of RNA Biology
Dongxiao Zhuang
Fudan University Huashan Hospital Department of Neurosurgery

Research Article

Keywords: Microglial metabolism, Metabolic reprogramming, Tumor Treating Fields, Ferroptosis

Posted Date: September 22nd, 2026

DOI: https://doi.org/10.21203/rs.3.rs-10927434/v1

License: This work is licensed under a Creative Commons Attribution 4.0 International License.
Read Full License

Abstract

Background

Metabolic plasticity is a hallmark of glioblastoma (GBM), sustaining tumor growth, redox balance, and therapy resistance through dynamic interactions between malignant cells and tumor-associated myeloid cells. Whether Tumor Treating Fields (TTF) remodel metabolism across these cellular compartments and thereby alter metabolic vulnerability in glioma cells remains unknown.

Methods

Patient-derived glioblastoma organoids were subjected to single-cell transcriptomic analysis after TTF exposure to characterize cell-type-specific responses. The direct effects of TTF on microglia were further examined in isolated BV2 cells and primary murine and human microglia. Microglial antitumor activity was assessed using conditioned-medium transfer, clonogenic and migration assays, and patient-derived organoids. Glycolytic involvement was evaluated using 2-deoxy-D-glucose, while ferroptosis-associated injury in recipient glioma cells was assessed by transcriptomic, biochemical, ultrastructural, and pharmacological analyses.

Results

TTF simultaneously suppressed mitotic programs in malignant cells and induced coordinated immune, secretory, and metabolic remodeling in microglia. Similar responses were reproduced in isolated murine and human microglia in the absence of tumor cells, establishing microglia as a direct target of TTF. After field withdrawal, TTF-primed microglia retained antitumor activity and suppressed glioma-cell growth, clonogenicity, and migration. Conditioned medium from human microglia also reduced proliferation in patient-derived glioblastoma organoids. TTF induced an HIF-1α-associated glycolytic program in microglia, and inhibition of glucose metabolism with 2-deoxy-D-glucose attenuated the antitumor activity of subsequently collected conditioned medium. In recipient glioma cells, the microglial secretome altered glutathione and lipid-redox programs, increased lipid peroxidation and Fe^{2+} accumulation, and induced mitochondrial and pharmacological changes consistent with ferroptosis-associated oxidative injury.

Conclusions

TTF induces a previously unrecognized metabolic response in microglia that contributes to glioma suppression after field withdrawal. By linking TTF-induced microglial glucose metabolism to redox disruption and ferroptotic vulnerability in neighboring glioma cells, these findings expand the biological

effects of TTF beyond direct antimitotic activity and reveal a multicellular metabolic mechanism within the glioblastoma microenvironment.

Introduction

Metabolic plasticity is a central feature of glioblastoma (GBM), enabling malignant cells to maintain energy production, biosynthesis, and redox balance despite spatial variation in oxygen and nutrient availability. Although enhanced glycolysis is a prominent feature of GBM, these tumors can also use alternative substrates and metabolic pathways, including acetate oxidation and lipid acquisition, to sustain their growth (Mashimo et al., 2014; Kloosterman et al., 2024). Increasing evidence further indicates that metabolic adaptation in GBM is not confined to malignant cells. Nonmalignant cells within the tumor microenvironment can supply metabolites to glioma cells and can themselves undergo metabolic remodeling in response to tumor-derived signals. Tumor metabolism in GBM therefore represents a multicellular process in which malignant and stromal or immune compartments collectively shape nutrient utilization, redox homeostasis, and therapeutic response.

Microglia and monocyte-derived macrophages constitute a major component of the GBM microenvironment and are important participants in this metabolic network (Klemm et al., 2020). Their metabolic state is closely linked to their immune and tumor-regulatory functions. In microglia, oxidative stress–dependent NR4A2–SQLE signaling disrupts cholesterol homeostasis and limits antigen presentation, whereas in monocyte-derived macrophages, tumor-induced glycolysis and lactate-dependent histone lactylation promote IL-10 production and T-cell suppression (Ye et al., 2023; De Leo et al., 2024). Glioma-associated macrophages can also recycle myelin-derived lipids and transfer them to glioma cells, directly supporting the metabolic demands of mesenchymal tumors (Kloosterman et al., 2024). These findings establish glioma-associated myeloid cells as both responders to and regulators of metabolic signals within GBM. Whether a therapeutic intervention can directly reprogram this myeloid metabolic state and convert it into an antitumor response remains poorly understood.

TTF is a clinically established physical therapy for GBM whose antitumor activity has traditionally been attributed to disruption of mitosis and induction of tumor-cell stress. More recent studies have shown that TTF also activates inflammatory signaling, including the cGAS–STING and AIM2 pathways (Chen et al., 2022), suggesting biological effects beyond mitotic interference. TTF may additionally influence tumor metabolism. In human GBM cells, TTF reduces PKM2 expression and suppresses PKM2-associated glycolytic activity (Patel et al., 2021). However, these metabolic effects have been examined primarily in malignant cells. Whether TTF induces distinct metabolic responses in tumor-associated immune cells, particularly microglia, remains unknown. More importantly, it is unclear whether such metabolic remodeling contributes to microglial antitumor activity or influences redox homeostasis and ferroptotic vulnerability in neighboring glioma cells.

Here, we used patient-derived glioblastoma organoids (GBOs), which retain key cellular and molecular features of their parental tumors, to examine the effects of TTF across malignant and myeloid

compartments at single-cell resolution (Jacob et al., 2020). TTF suppressed mitotic programs in glioma cells while inducing broad immune, secretory, and metabolic remodeling in microglia. Experiments in isolated BV2 cells and primary murine and human microglia demonstrated that this response could be initiated directly by TTF in the absence of tumor cells. TTF-exposed microglia retained antitumor activity after field withdrawal and released soluble factors that suppressed glioma-cell growth and migration. Mechanistically, TTF induced HIF-1α-associated glycolytic remodeling in microglia, whereas inhibition of glucose metabolism reduced the antitumor activity of the resulting conditioned medium. In recipient glioma cells, this secreted response altered glutathione and lipid-redox programs and promoted ferroptosis-associated oxidative injury. Together, these findings reveal a previously unrecognized metabolic dimension of TTF action in which metabolic remodeling of microglia is linked to redox disruption in neighboring glioma cells, extending the effects of TTF from direct tumor-cell injury to metabolic interactions within the glioblastoma microenvironment.

Methods

Cell culture

The murine glioma cell lines GL261 (RRID: CVCL_Y003) and CT2A (RRID: CVCL_ZJ44) and the murine microglial cell line BV2 (RRID: CVCL_0182) were obtained from the Cell Bank of the Chinese Academy of Sciences (Shanghai, China). Cells were maintained in DMEM/F12 supplemented with 10% fetal bovine serum at 37°C in a humidified incubator containing 5% CO_2. Cell-line identities were authenticated by short tandem repeat profiling within 6 months of use, and cultures were routinely confirmed to be free of mycoplasma contamination.

Isolation and culture of primary microglia

Primary microglia were isolated from postnatal day 0–2 C57BL/6 mice. After euthanasia, the neonatal mice were surface-disinfected in 75% ethanol for 5 min. Cerebral hemispheres were isolated, minced into approximately 1-mm pieces and mechanically dissociated. The suspension was passed through a 70-μm strainer, centrifuged at 1,500 rpm for 5 min and seeded into dishes precoated with 0.1 mg/mL poly-L-lysine. Mixed glial cultures were maintained in DMEM/F12 containing 10% fetal bovine serum, with medium replacement on days 4 and 8.

On days 9–10, loosely adherent microglia were collected by orbital shaking at 180 rpm for 40 min and centrifuged at 1,500 rpm for 5 min. The cells were reseeded into 24-well plates. On the following day, the medium was replaced with a 1:1 mixture of fresh microglial medium containing 0.1 μg/mL M-CSF and astrocyte-conditioned medium, and the cells were cultured for a further 2–3 days before use.

TTFields treatment

BV2 cells, primary microglia and glioblastoma organoids (GBOs) were exposed to TTFields using the inovitro™ system (Novocure) at 200 kHz and 1.4 V/cm under standard culture conditions (37°C and 5%

CO_2). BV2 cells and primary microglia were seeded onto 24-mm coverslips at 6×10^4 and 1×10^5 cells per coverslip, respectively, and allowed to adhere overnight. GBOs were maintained in suspension at 5–6 organoids per well.

BV2 cells and primary microglia were exposed for 24 h in short-term phenotypic and functional assays and for 40 h in prolonged priming, conditioned-medium and secretome experiments. GBOs were exposed for 40 h. Parallel cultures maintained in the same system without field application served as matched controls.

Phagocytosis assay

BV2 cells and primary microglia were seeded onto glass coverslips at 2×10^5 cells per well and exposed to TTFields for 24 h. Cells were then incubated for 2 h at 37°C in a non-CO_2 incubator with pHrodo™ Green E. coli BioParticles™ conjugate (Thermo Fisher Scientific, P35366) prepared at 1 mg/mL in serum-free Opti-MEM. After washing, intracellular fluorescence was imaged by Leica confocal microscopy. Phagocytosis-positive cells were quantified in at least three random fields per coverslip. Each condition included three technical replicates, and the experiment was independently repeated three times.

Transwell migration assay

GL261 and CT2A cells were seeded in the upper inserts of 24-well Transwell plates with 8.0-μm pores (Corning, 3844) at 5×10^4 and 3×10^4 cells per insert, respectively. Primary microglia on coverslips were exposed to TTFields for 24 h and transferred intact to the lower chambers containing 1 mL fresh serum-free medium. After 24 h of co-culture, non-migrated cells were removed from the upper membrane surface. Migrated cells were fixed, stained with 0.1% crystal violet and quantified in five random fields per insert using ImageJ.

Glioma-cell viability assay

Relative glioma-cell viability was assessed using the Cell Counting Kit-8 (CCK-8; TargetMol). GL261 and CT2A cells were seeded in 96-well plates at 2,500 and 1,500 cells per well, respectively, and allowed to adhere overnight. The medium was replaced with the indicated treatment or conditioned medium. At the specified time points, 10 μL CCK-8 reagent was added per well and incubated for 2 h at 37°C. Absorbance at 450 nm was measured using a Synergy HTX microplate reader (BioTek Instruments), background-subtracted and normalized to the corresponding control.

Preparation of conditioned media

During TTFields treatment, culture dishes were sealed with Parafilm to limit evaporation, and fresh medium was added every 24 h. Matched untreated cell cultures and cell-free medium incubated under otherwise identical conditions served as controls. Conditioned medium (CM) was collected at the designated endpoint and used for downstream experiments.

For temozolomide-induced microglial CM, BV2 cells were treated with 100 or 200 μM temozolomide for 24 h, washed three times with PBS and incubated in fresh DMEM for 48 h before CM collection. To generate glioma-conditioned BV2 cells (BV2-GAM), GL261 CM was passed through a 0.45-μm filter, mixed 1:1 with fresh medium and applied to BV2 cells for 48 h. For flow-cytometric assessment of glioma-derived effects, BV2-GAM cells were cultured with 30% GL261 CM.

GBO culture

Fresh tissue was transported in ice-cold Hibernate-A medium (Thermo Fisher Scientific). Viable, tumor-rich, gray and relatively dense regions were selected, whereas normal brain, edematous, necrotic, hemorrhagic and loose regions were removed. A portion of the parental tumor was retained for histology and sequencing. The remaining tissue was washed three times with DMEM/F12 and incubated in 10 mL red blood cell lysis buffer (Yeasen, 40401ES72) for 10 min at 37°C and 100 rpm. After washing, the tissue was cut under a stereomicroscope into approximately 0.5-mm pieces.

Four to five tissue pieces were placed in each well of an ultra-low-attachment 24-well plate containing 1 mL GBO medium and cultured at 37°C with 5% CO_2 on an orbital shaker at 120 rpm. GBO medium comprised 50% DMEM/F12, 50% Neurobasal medium, 1× GlutaMAX, 1× nonessential amino acids, 1× penicillin–streptomycin, 1× N2, 1× B27 without vitamin A, 1× 2-mercaptoethanol and 2.5 μg/mL human insulin. Half of the medium was replaced every 2 days. After 1–2 weeks, rounded organoids with dense centers and smooth edges were retained for experiments.

Preparation of GBO single-cell suspensions

Approximately 20–30 control or TTFields-treated GBOs per group were maintained in GBO medium at 4°C until processing, washed three times with PBS and minced on ice into approximately 1-mm^3 pieces. Samples were digested with papain (Worthington Biochemical Corporation; CAS 9001-73-4) for 15 min at 37°C, passed through a 70-μm strainer and centrifuged at 300 × g for 5 min at 4°C. Red blood cells were lysed, and dead cells were removed using the Dead Cell Removal Kit (Miltenyi Biotec, 130-090-101). Cell number and viability were assessed by AO/PI staining. Samples with viability > 90%, > 5 × 10^4 total cells, > 50% nucleated cells and < 30% cell aggregates were used for single-cell sequencing. For cytokine profiling, CD11b-positive cells were enriched using CD11b MicroBeads (Miltenyi Biotec, 130-049-601) and processed for protein extraction.

Single-cell RNA sequencing and analysis

Single-cell libraries were prepared using the Chromium Next GEM Single Cell 3' Gene Expression v3.1 workflow (10x Genomics) and sequenced on an Illumina NovaSeq 6000. Gene–barcode matrices were generated with Cell Ranger v10.1.0 against GRCh38 and analyzed in Seurat v5.5.0. After removal of low-quality cells and doublets, the data were normalized, integrated, clustered and visualized by principal component analysis and UMAP. A total of 51,917 cells were retained. Cell types were annotated using canonical markers, malignant glioma cells were identified from inferred copy-number profiles using

inferCNV, and the GBO-associated myeloid compartment was subclustered for state and pathway analyses.

Flow cytometry

Control and TTFields-treated BV2 cells and primary microglia were detached with EDTA-free trypsin, washed and stained for 30 min at 4°C with antibodies against CD86, PD-L1, CD206, PD-1, MHC-I and MHC-II. Antibody information is provided in Table S3. Data were acquired on a five-laser Cytek Aurora full-spectrum flow cytometer and analyzed in FlowJo v10.8.1. Debris, doublets and nonviable cells were excluded, and marker expression was reported as median fluorescence intensity.

RNA extraction and quantitative RT-PCR

Total RNA was extracted from BV2 cells and primary microglia using the HiPure Total RNA Plus Kit (Magen, R4111) and reverse-transcribed using HiScript III RT SuperMix for qPCR with gDNA wiper (Vazyme, R323-01). Quantitative PCR was performed using ChamQ Blue Universal SYBR qPCR Master Mix (Vazyme, Q312-02). Relative expression was calculated using the 2^−ΔΔCt method with Actb as the reference gene. Primer sequences are listed in Table S3. BV2 cells treated with 100 ng/mL lipopolysaccharide for 24 h served as an inflammatory-response benchmark.

Immunofluorescence staining of GBOs

Control and TTFields-treated GBOs were fixed in 4% paraformaldehyde, cryoprotected in 30% sucrose, embedded in OCT and cut into 10-μm cryosections. Sections were permeabilized, blocked and incubated overnight at 4°C with antibodies against IBA1, CD86 and CD163, followed by fluorescent secondary antibodies and DAPI. Confocal images were quantified using ImageJ, and the proportions of IBA1-positive cells coexpressing CD86 or CD163 were calculated.

Bulk RNA sequencing and pathway analysis

Total RNA was collected from control and TTFields-treated BV2 cells and primary microglia. In a separate experiment, GL261 cells were collected after 12 h of exposure to CM from control or TTFields-primed primary microglia. Poly(A)-selected libraries were sequenced on an Illumina HiSeq X Ten. Reads were aligned to the mouse GRCm38/mm10 genome using STAR, gene counts were generated using featureCounts, and differential expression was analyzed using DESeq2. GO, KEGG and Reactome enrichment and gene set enrichment analysis were performed using clusterProfiler, and pathway-level variation was assessed using GSVA. P values were adjusted using the Benjamini–Hochberg method.

Multiplex cytokine profiling

Cytokines and chemokines were measured using a Luminex 200 system according to the manufacturer's instructions. Four GBO-derived CD11b-positive cell lysates per group were analyzed using a human 40-analyte chemokine/cytokine panel (LabEx, LXLBH40-1), and values were normalized to total protein.

Primary-microglia supernatants from three independent cultures per group were analyzed using a mouse 31-analyte panel (LabEx, LX-MultiD-31) and normalized to viable-cell number. One primary-microglial sample was re-assayed for technical reasons, and the repeat value was used in the final analysis.

OVA-derived peptide–MHC-I display assay

After control or TTFields exposure, BV2 cells and primary microglia were pulsed with SIINFEKL peptide ($OVA_{257–264}$; 10 μg/mL) for 24 h. Cells were washed and stained with an antibody recognizing SIINFEKL–H-2K□ complexes, followed by flow-cytometric analysis. No-peptide and unstained samples served as controls. Peptide–MHC-I display was reported as median fluorescence intensity.

Conditioned-medium transfer experiments

CM was collected from control or TTFields-treated BV2 cells and primary microglia after 40 h, centrifuged to remove cellular material and transferred to GL261 or CT2A cells. The collection volume was normalized to culture area. When temozolomide, 2-deoxy-D-glucose (2-DG) or other compounds were used during microglial pretreatment, cells were washed and incubated in fresh drug-free medium before CM collection.

Orthotopic GL261-luciferase co-implantation model

Male C57BL/6 mice aged 4–6 weeks were randomly assigned to experimental groups. GL261-luciferase cells were mixed with untreated primary microglia or primary microglia pre-exposed to TTFields (200 kHz, 1.4 V/cm for 40 h). Each mouse received 2 × 10^5 GL261-luciferase cells and 2 × 10^5 BV2 cells in 3 μL by stereotactic intracranial injection at 2.5 mm right lateral, 1.5 mm anterior and 3.5 mm ventral to bregma. Tumor burden was monitored by bioluminescence imaging, and survival was assessed using prespecified humane endpoints. Mice did not receive TTFields after implantation.

Ferroptosis-associated assays

GL261 and CT2A cells were exposed to the indicated CM for 24 h. Lipid reactive oxygen species were measured after staining with BODIPY 581/591 C11 (Invitrogen, D3861; 1:1,000 dilution) for 15 min at room temperature and analyzed by flow cytometry. Intracellular Fe^{2+} in GL261 cells was measured using FerroOrange (Dojindo Laboratories, F374), and cellular GSH and GSSG were measured using the GSH/GSSG Assay Kit (Beyotime, S0053), according to the manufacturers' instructions. Rescue experiments used ferrostatin-1 (10 μM), necrostatin-1 (2 μM), Z-VAD-FMK (10 μM) and N-acetylcysteine (5 μM). Relative viability was assessed by CCK-8, with inhibitor-alone controls included.

Western blotting

Cells were lysed in SDS sample buffer containing protease and phosphatase inhibitors. Equal amounts of protein were separated by SDS-PAGE, transferred to PVDF membranes and incubated with antibodies against HIF-1α, total mTOR, phospho-mTOR and actin. Signals were detected using HRP-conjugated

secondary antibodies and chemiluminescence. Band intensities were quantified using ImageJ; target proteins were normalized to actin, and phospho-mTOR was additionally normalized to total mTOR.

2-Deoxy-D-glucose treatment

BV2 cells or primary microglia were treated with 2 μM 2-DG during 24 h of TTFields exposure. Cells were washed twice with PBS and incubated in fresh 2-DG-free medium for 48 h. The collected medium was transferred to GL261 or CT2A cells as described above.

Statistical analysis

Data are presented as mean ± SD. Two groups were compared using an unpaired two-tailed Student's t test or Welch's t test when variances were unequal; multiplex-analyte comparisons used Welch's t test. Multiple groups were analyzed by one-way or two-way ANOVA followed by an appropriate multiple-comparison test, including Dunnett's test for comparisons with a single control. Survival was analyzed using the Kaplan–Meier method and log-rank test. Transcriptomic and multiplex-analyte P values were adjusted using the Benjamini–Hochberg method, with adjusted $P < 0.05$ considered significant. Analyses were performed using GraphPad Prism 10 and R v4.6.1.

Results

Single-cell transcriptomics reveals coordinated glioma and microglial responses to TTFields in glioblastoma organoids

To establish a model that preserved both the tumor compartment and resident myeloid populations, we generated patient-derived glioblastoma organoids (GBOs) from freshly resected tumor tissues. The tissues formed compact three-dimensional organoids during culture (Fig. S1A), and histological comparison showed preservation of major morphological features between the parental tumors and matched GBOs (Fig. S1B). Genomic profiling further demonstrated substantial conservation of somatic alterations between the parental tumor and corresponding GBO (Fig. S1C). Immunofluorescence staining revealed Ki-67$^+$ proliferative cells and retained IBA1$^+$ myeloid cells within the organoids. Glioma-associated and stem-like markers, including SOX2, Nestin, and NOTCH1, also remained readily detectable (Fig. S1D). Together, these findings confirmed that the GBOs preserved key histological, genomic, and cellular characteristics of the parental tumors, supporting their use for evaluating multicellular responses to TTFields.

Using this validated model, we examined how TTFields reshape cellular states within the glioblastoma microenvironment. GBOs derived from two patients were exposed to TTFields at 1.4 V/cm for 40 h, with matched untreated organoids serving as controls. The organoids were subsequently dissociated and subjected to 10x Genomics single-cell RNA sequencing (Fig. 1A).

After quality control, 51,917 cells were retained for downstream analysis. UMAP clustering followed by canonical-marker annotation identified glioma cells, microglia, macrophages, oligodendrocytes, T cells, endothelial cells, and a small unclassified population (Fig. 1B and Fig. S1E). Glioma cells constituted the predominant population, whereas microglia and macrophages represented the major immune compartments and T cells were scarce. Cells from both control and TTFields-treated GBOs were represented across the major populations, enabling cell-type-resolved analysis of the transcriptional response to TTFields.

Because disruption of mitosis is an established biological effect of TTFields, we first analyzed the glioma-cell compartment to determine whether the GBO model captured the expected tumor-cell response. Differential expression analysis identified 3,057 upregulated and 2,370 downregulated genes following TTFields treatment (Fig. 1C). KEGG analysis of the upregulated genes revealed enrichment of cytokine–cytokine receptor interaction, chemokine signaling, MAPK signaling, NF-κB signaling, and IL-17 signaling pathways (Fig. 1D). In parallel, GO analysis of the downregulated genes consistently highlighted processes associated with mitotic progression, including metaphase–anaphase transition, sister chromatid segregation, chromosome and kinetochore organization, and mitotic spindle checkpoint signaling (Fig. 1E). These findings demonstrate that TTFields suppressed core mitotic machinery while inducing inflammatory and chemokine-related signaling within glioma cells. Recovery of the canonical antimitotic response provided additional internal validation that the GBO model captured biologically relevant effects of TTFields.

Having established the expected response in glioma cells, we focused on microglia, the principal immune population of interest. Differential expression analysis identified 2,056 upregulated and 613 downregulated genes in TTFields-treated microglia (Fig. 1F). Among the prominently induced genes were *CXCL8*, *CXCL1*, *CXCL5*, *IL1B*, and *S100A9*, indicating enhanced inflammatory and chemokine-associated activity. KEGG analysis placed cytokine–cytokine receptor interaction among the most strongly enriched pathways, together with PI3K–Akt signaling, chemokine signaling, NOD-like receptor signaling, IL-17 signaling, and TNF signaling (Fig. 1G).

Consistent with these pathway-level changes, TTFields-treated microglia exhibited an increased inflammatory module score and a modest reduction in the immunoregulatory module score (Fig. 1H). Representative inflammatory genes, including *CXCL8* and *IL1B*, were increased, whereas *IDO1* and *IGFBP2*, included in the immunoregulatory module, were reduced. GSEA further supported enrichment of the innate immune system program following TTFields exposure (Fig. 1I).

Together, these analyses reveal coordinated but cell-type-specific responses to TTFields within GBOs, characterized by suppression of mitotic programs in glioma cells and activation of inflammatory and innate immune programs in microglia. These findings identify microglia as a major TTFields-responsive immune population within the organoid microenvironment and provide the rationale for subsequently determining whether TTFields directly reprogram microglial activation and effector functions.

TTFields directly reprogram microglial phenotype and function

To determine whether the myeloid changes observed in TTFields-treated GBOs reflected a direct response of microglia to TTFields, we examined BV2 cells and primary microglia (pMG) under the same treatment conditions. Purified pMG cultures showed high CD11b enrichment, and TTFields did not significantly affect pMG cell numbers, indicating no evident cytotoxicity under these conditions (Fig. S2A, B). Morphologically, both BV2 cells and pMG shifted from a predominantly elongated or spindle-like appearance toward a more rounded, amoeboid morphology after TTFields treatment, consistent with a transition toward an activated state (Fig. S2C, D) [1]. This was accompanied by marked induction of Il1b, Cd86, and Nos2 in both models (Fig. 2A, B).

To place this gene-expression pattern in context, LPS was included as a positive control for robust inflammatory activation. Notably, Tnf and Il6 were not significantly increased by TTFields (Fig. S2E), whereas LPS induced a broader inflammatory response across the examined genes (Fig. S2F). Compared with LPS, TTFields preferentially induced Il1b, Cd86, and Nos2, indicating a more selective pattern of microglial activation rather than generalized inflammatory stimulation.

Flow-cytometric analysis further supported this phenotypic shift. TTFields increased surface CD86 while reducing PD-L1 in both BV2 cells and pMG (Fig. 2C, D). In GBOs, TTFields also altered the proportion of CD163-positive cells within the IBA1-positive myeloid compartment (Fig. 2E), further supporting remodeling of the myeloid phenotype across experimental systems.

We further assessed whether these phenotypic changes were accompanied by alterations in microglial immune function. Total surface MHC-I was not globally increased by TTFields, showing a reduction in BV2 cells and no significant increase in pMG (Fig. S2G, H). In contrast, surface OVA–MHC-I complexes increased after TTFields treatment (Fig. 2F, G). Thus, enhanced antigen-specific MHC-I presentation occurred without a corresponding increase in total MHC-I abundance, supporting an improvement in antigen-presenting function rather than generalized MHC-I upregulation.

Phagocytosis was then evaluated as another key effector function of microglia. TTFields-treated pMG showed increased uptake of fluorescent beads, as measured by bead-positive area normalized to IBA1-positive cell number (Fig. 2H), and a similar increase was observed in BV2 cells (Fig. S2I). Collectively, these findings show that TTFields directly reprograms microglia toward a distinct immune-activated state characterized by coordinated phenotypic changes, enhanced antigen presentation, and increased phagocytic capacity. Rather than inducing a uniform inflammatory response, TTFields appears to drive a selective functional reprogramming of microglia.

TTFields remodels microglial cytokine programs

Having established by qPCR and flow cytometry that TTFields altered microglial activation markers, we next examined the broader transcriptional response. Bulk RNA sequencing identified 2,211 upregulated

and 1,842 downregulated genes in BV2 cells and 1,368 upregulated and 1,964 downregulated genes in primary microglia following TTFields exposure (Figs. 3B and 3C). Across both models, TTFields induced inflammatory genes such as *Ptgs2*, *Il1b*, *Nos2*, and *Cxcl3*, while reducing selected antigen-processing and myeloid-associated genes, including *Tap1*, *Psmb9*, *Trem2*, *Fcgr3*, and *Itgam*. *Mrc1* was additionally reduced in primary microglia. Gene-expression changes were positively correlated between the two models (Pearson's $r = 0.444$), indicating a shared core response together with model-specific differences (Fig. 3D).

Pathway analysis placed cytokine regulation among the highest-ranked responses to TTFields. In BV2 cells, cytokine–cytokine receptor interaction was among the most significantly enriched upregulated pathways, together with TNF and IL-17 signaling. Cytokine-associated processes were likewise prominent in primary microglia, with enrichment extending to homeostatic feedback programs that regulate the magnitude and duration of cytokine production (Figs. 3E and 3F). These findings suggested that TTFields did not uniformly increase or suppress cytokine expression but instead broadly remodeled the cytokine regulatory network.

Guided by these pathway-level findings, we next examined cytokine-related transcripts in greater detail. TTFields increased multiple chemokine genes, including *Cxcl3*, *Cxcl2*, *Ccl2*, *Ccl5*, and *Ccl3*, together with inflammatory genes such as *Il1b*, *Tnf*, *Nos2*, and *Ptgs2*. Although the magnitude and pattern of these changes differed between BV2 cells and primary microglia, both models showed broad reorganization of cytokine-related gene expression (Fig. 3G).

To determine how these transcriptional changes were reflected at the protein level, we profiled cytokines in $CD11b^+$ cells isolated from control and TTFields-treated GBOs and in culture supernatants collected from control and TTFields-treated primary microglia (Fig. 3H). In GBO-derived $CD11b^+$ cells, TTFields increased the inflammatory cytokines IL-1β, IL-6, TNF-α, and GM-CSF, together with the chemotactic mediators CXCL8, CXCL5, CCL20, and CXCL1. Cytokines involved in immune-cell trafficking and spatial organization, including CXCL12 and CCL19, were also increased, whereas CXCL9 was reduced and CCL2 remained unchanged (Fig. 3I). Thus, the response was not a nonspecific increase in cytokine abundance but a selective shift toward an inflammatory and chemotactic signaling profile. Importantly, this pattern was observed in human GBO-derived $CD11b^+$ cells, extending the transcriptional findings from isolated microglial cultures to the organoid-associated myeloid compartment.

Across 28 cytokines shared between the GBO and primary microglial datasets, several inflammatory and chemotactic mediators changed in the same direction, although the overall association was modest and did not reach statistical significance (Spearman's $r = 0.29$, $P = 0.13$; Figure XJ). The incomplete correspondence indicated that the precise composition of the cytokine response remained dependent on the cellular model and biological compartment. Nevertheless, the convergent transcriptomic and protein-level findings supported a shift of microglia toward a cytokine-active state with an enhanced capacity to modify inflammatory signaling and immune-cell recruitment within the local microenvironment. Because

these cytokine changes alone could not establish whether the remodeled microenvironment was functionally antitumor, we next directly tested the effects of TTFields-primed microglia on glioma cells.

TTFields-primed microglia exert antitumor effects against glioma

We next examined whether TTFields-induced microglial reprogramming translated into antitumor activity against glioma cells. Conditioned medium (CM) was collected from TTFields-treated BV2 cells and primary microglia (pMGs) and transferred to glioma cells (Fig. 4A). CM from TTFields-primed BV2 cells progressively reduced glioma-cell viability over 24–72 h (Fig. 4B). A similar effect was observed when BV2 cells were first conditioned with GL261-derived CM to generate a GAM-like state, indicating that TTFields retained its ability to induce a tumor-suppressive microglial phenotype in a glioma-associated context. Consistently, CM from TTFields-primed pMGs produced a comparable time-dependent suppression of glioma-cell viability (Fig. 4C).

To exclude a direct effect of TTFields exposure on the culture medium, cell-free medium was exposed to TTFields in parallel. This medium had little effect on glioma cells, whereas CM from TTFields-primed pMGs markedly reduced glioma-cell viability (Fig. 4D), supporting a microglia-dependent antitumor effect. We next compared TTFields with conventional cytotoxic treatment. In contrast to TTFields-primed microglia, CM from TMZ-treated BV2 cells did not suppress glioma cells and instead increased glioma-cell viability in a dose-dependent manner (Fig. 4E). These opposing responses further distinguish TTFields-induced microglial reprogramming from the myeloid response elicited by cytotoxic treatment.

We next assessed whether this suppressive effect was reflected in sustained tumor growth. CM from TTFields-primed pMGs or BV2 cells markedly reduced colony formation in both GL261 and CT2A cells, whereas TTFields-exposed cell-free medium produced only a limited effect (Fig. 4F). We further tested this activity in a human glioma model by transferring CM from TTFields-primed human microglial cells (hMCs) to glioblastoma organoids (GBOs). EdU incorporation was markedly decreased in GBOs exposed to TTFields-hMC-CM compared with control hMC-CM (Fig. 4G, H), demonstrating that the growth-suppressive effect was also evident in a human three-dimensional tumor model.

We then asked whether the antitumor activity persisted after TTFields withdrawal. Control or TTFields-primed microglia were replated in fresh medium in the lower chamber of an indirect Transwell co-culture system, with CT2A cells seeded in the upper inserts. TTFields-primed microglia markedly reduced CT2A migration compared with control microglia (Fig. 4I). Thus, the altered microglial state remained functionally active after removal of the field and continued to suppress glioma-cell motility.

Finally, we examined whether this retained antitumor activity could also be detected in the intracranial tumor environment. GL261-luc cells were orthotopically co-implanted with either untreated pMG cells or pMG cells pre-exposed to TTFields, thereby isolating the contribution of the pre-established microglial state from ongoing field exposure. Bioluminescence imaging on day 14 revealed substantially lower intracranial tumor burden in mice receiving TTFields-primed pMG cells than in those receiving untreated

pMG cells (Fig. 4J). Together, these findings show that TTFields establish a transferable tumor-suppressive microglial state that persists beyond the period of field exposure and restricts glioma growth and migration across murine, human organoid, and intracranial models.

TTFields-primed microglia promote ferroptosis-associated oxidative injury in glioma cells

Having established that TTFields-primed microglia suppress glioma cells, we investigated how this cytotoxic effect was mediated. Conditioned medium (CM) was collected from control or TTFields-treated primary microglia and transferred to GL261 cells (Fig. 5A). Recipient tumor cells were then subjected to bulk RNA sequencing and complementary functional analyses.

Bulk RNA sequencing revealed clear transcriptomic separation between GL261 cells exposed to control pMG-CM and those exposed to TTFields-pMG-CM (Fig. S5A). GSEA showed positive enrichment of ferroptosis, glutathione metabolism, arachidonic acid metabolism, and biosynthesis of unsaturated fatty acids (Fig. 5B and Fig. S5C). Ferroptosis showed positive but borderline enrichment (NES = 1.57, FDR = 0.074), whereas glutathione metabolism was significantly enriched (NES = 1.79, FDR = 0.014). In contrast, neither apoptosis nor necroptosis showed corresponding positive transcriptional enrichment. Sample-level pathway analysis further demonstrated increased activity of lipid-redox and antioxidant-response programs (Fig. S5D). Gene-level analysis likewise revealed coordinated changes in iron acquisition and retention, lipid oxidation, ferroptosis-defense systems, and adaptive antioxidant responses (Fig. 5C). Collectively, these transcriptomic findings implicated ferroptosis-associated lipid-redox stress as a potential mechanism of tumor-cell injury and motivated targeted functional validation.

Exposure to TTFields-pMG-CM caused pronounced morphological deterioration in GL261 cells, characterized by reduced cell density, loss of cellular spreading, cell rounding and contraction, membrane distortion, detachment, and accumulation of cellular debris (Fig. 5D). Cell-free medium exposed to TTFields under otherwise matched conditions produced substantially milder changes, arguing against direct field exposure of the medium as the principal cause of injury. Although these morphological features were not specific to ferroptosis, they supported a microglia-dependent cytotoxic effect consistent with the transcriptomic evidence of lipid-redox stress.

We therefore directly assessed iron accumulation, lipid peroxidation, and cellular redox homeostasis. Compared with the corresponding control CM, both TTFields-pMG-CM and TTFields-BV2-CM markedly increased lipid ROS and intracellular Fe^{2+} in GL261 cells (Fig. 5E and Fig. 5F). These changes were accompanied by increased MDA levels and a pronounced reduction in the GSH/GSSG ratio, indicating enhanced lipid peroxidation and impaired antioxidant capacity (Fig. 5G and Fig. 5H). LPS-CM, included as an inflammatory reference, did not reproduce this lipid-redox phenotype. These findings suggested that TTFields induced a distinct microglial secretory program that promoted iron accumulation and lipid-oxidative injury in glioma cells, rather than merely recapitulating a generalized inflammatory state. This

phenotype was independently reproduced in CT2A cells, in which TTFields-pMG-CM and TTFields-BV2-CM induced marked morphological deterioration and increased lipid ROS (Fig. S5B and Fig. S5E).

To determine whether this lipid-peroxidative phenotype extended beyond monolayer tumor-cell cultures, we examined 4-hydroxy-2-nonenal (4-HNE) immunoreactivity in patient-derived organoids and paired clinical specimens. In paired glioblastoma specimens from seven patients, post-TTFields tissues generally displayed more prominent 4-HNE staining than the corresponding pretreatment specimens, although the magnitude and spatial distribution of the staining varied among patients (Fig. S6A). Similarly, both GBO1 and GBO2 showed more extensive 4-HNE immunoreactivity following ex vivo TTFields exposure than their respective untreated controls (Fig. S6B). These tissue-level observations extended the cell-based findings and indicated that TTFields treatment was accompanied by enhanced lipid peroxidation in both patient-derived glioblastoma organoids and clinical glioblastoma specimens.

We next examined whether this lipid-peroxidative stress was accompanied by disruption of the core GPX4-dependent defense system. GPX4 protein abundance was markedly reduced in GL261 cells exposed to either TTFields-pMG-CM or TTFields-BV2-CM (Fig. 5I). Thus, despite the transcriptional induction of adaptive antioxidant programs, recipient glioma cells failed to preserve a central defense against phospholipid peroxidation. Transmission electron microscopy provided complementary evidence of organelle stress following TTFields-pMG-CM treatment (Fig. 5J). Treated cells displayed irregular mitochondrial profiles and disrupted mitochondrial internal architecture (blue arrows), together with dilation and disorganization of endoplasmic reticulum cisternae (yellow arrows). Although not diagnostic of ferroptosis in isolation, these ultrastructural abnormalities were consistent with extensive oxidative organelle injury.

Finally, we determined whether lipid peroxidation contributed directly to the cytotoxic response. GL261 cells were pretreated with inhibitors targeting distinct cell-death-associated processes before exposure to TTFields-pMG-CM (Fig. 5K). Ferrostatin-1 substantially restored cell viability, demonstrating that lipid-peroxidation-dependent ferroptotic injury was a causal contributor to the cytotoxic effect (Fig. 5L). NAC and Z-VAD-FMK also conferred marked protection, whereas necrostatin-1 produced a more limited rescue. These differential rescue effects suggested that broader oxidative stress and caspase-dependent cell death may operate alongside ferroptotic injury. Collectively, the transcriptomic, biochemical, tissue-level, ultrastructural, and pharmacological findings identify ferroptosis-associated oxidative injury as a prominent and functionally important component of the antitumor activity mediated by TTFields-primed microglia.

Glycolytic remodeling contributes to the antitumor activity of TTFields-primed microglia

To investigate how TTFields drives microglial reprogramming, we revisited the transcriptional changes induced by TTFields in BV2 cells and primary microglia (pMG). Pathway analysis highlighted metabolic remodeling as a shared feature of the response, with HIF-1 signaling and glycolysis-related programs

enriched in both models. In particular, GSEA showed positive enrichment of the glycolysis/gluconeogenesis pathway following TTFields exposure in both pMG and BV2 cells (Fig. 6A). Glycolysis module scores were also increased after TTFields treatment, reaching significance in BV2 cells and showing a similar trend in pMG (Fig. S6A). At the gene level, glycolysis-associated changes were broadly concordant between the two models, with all 11 shared glycolytic genes showing increased expression following TTFields exposure (Fig. S6B). Analysis of TTFields-treated GBOs further showed prominent glycolysis/gluconeogenesis activity across myeloid populations (Fig. S6C). **Such a metabolic shift is consistent with activated microglial states, in which increased reliance on glycolysis can support the heightened energetic and biosynthetic demands associated with immune activation** [2]. Together, these transcriptomic findings suggested that metabolic reprogramming, particularly enhanced glycolytic activity, may accompany the TTFields-induced microglial state.

We next examined this metabolic response experimentally. TTFields increased the expression of *Hif1a*, *Pkm2*, *Hk1*, and *Hk2* in both pMG and BV2 cells (Fig. 6B). At the protein level, TTFields induced time-dependent increases in HIF-1α, PFKFB3, and PKM2, together with increased mTOR abundance and phosphorylation (Fig. 6C,D). These changes supported coordinated activation of a glycolysis-associated metabolic program rather than isolated regulation of individual metabolic enzymes. This response was also distinguishable from conventional inflammatory stimulation. LPS produced little or no increase in several glycolysis-associated genes that were strongly induced by TTFields, including *Hif1a*, *Pkm2*, *Hk1*, and *Hk2* (Fig. S6D), indicating that the metabolic changes induced by TTFields were not simply a consequence of a broad LPS-like inflammatory response.

We then asked whether this glycolytic remodeling was functionally involved in the antitumor activity acquired by TTFields-primed microglia. Microglia were pretreated with 1 mM 2-deoxy-D-glucose (2-DG) before TTFields exposure, and conditioned medium was subsequently collected and transferred to glioma cells (Fig. 6E). Conditioned medium from TTFields-treated BV2 cells markedly reduced glioma-cell viability, whereas inhibition of glucose metabolism with 2-DG substantially attenuated this effect (Fig. 6F). A similar rescue was observed with conditioned medium derived from pMG (Fig. 6G). In contrast, 2-DG treatment alone had minimal effect on the activity of control microglial conditioned medium. These findings indicate that glycolytic remodeling contributes functionally to the TTFields-induced microglial state and is required for the full acquisition of its transferable antitumor activity.

Discussion

TTFields have been studied mainly as a tumor-cell-directed treatment that disrupts mitosis and induces stress responses in malignant cells[3]. This tumor-cell-centered view may overlook the myeloid compartment, which constitutes a major component of the immunosuppressive glioblastoma microenvironment and exhibits substantial phenotypic plasticity[4 5]. Reprogramming glioma-associated microglia/macrophages toward tumor-suppressive states has therefore emerged as an attractive therapeutic strategy, although its translation has been limited by the difficulty of achieving sustained and selective myeloid reprogramming within the tumor microenvironment [6–8]

A major strength of the present study is that the microglial response to TTFields was first identified by single-cell analysis of patient-derived glioblastoma organoids, rather than inferred from a cell-line model. Within the same human tumor-derived system, TTFields suppressed chromosome-segregation and spindle-checkpoint programs in glioma cells while broadly remodeling immune and metabolic programs in microglia. This simultaneous response suggested that microglia were not passive bystanders during treatment. Key features of the response were subsequently reproduced in isolated BV2 cells and primary murine and human microglia in the absence of tumor cells, demonstrating that microglia can respond directly to TTFields. Thus, the study progresses from an unbiased observation in patient-derived organoids to controlled validation across multiple experimental systems, supporting a broader view of TTFields as a treatment that acts on both glioma cells and the surrounding myeloid compartment.

The microglial response was selective rather than a nonspecific inflammatory reaction. TTFields increased CD86, reduced PD-L1, and enhanced phagocytosis and OVA peptide–MHC-I complex formation, whereas total MHC expression and TNF-α production showed limited or variable changes. This pattern argues against a simple M1/M2 interpretation and is more consistent with the heterogeneous and multidimensional states of glioblastoma-associated microglia[9]. More importantly, the response converged at the functional level. Across BV2 cells and primary murine and human microglia, TTFields treatment increased the ability of microglia to suppress glioma-cell growth, clonogenicity, and migration. This antitumor activity was also retained after conditioning with glioma-cell-derived factors, indicating that TTFields can redirect microglial function even in a tumor-associated context. The central finding is therefore not the induction of a single activation marker, but the acquisition of a reproducible antitumor function.

A particularly distinctive feature of this response was that it persisted after TTFields exposure had ended. Conditioned medium from TTFields-treated microglia remained active against glioma cells, and pre-exposed microglia continued to suppress tumor cells after transfer into fresh medium in a field-free Transwell system. By contrast, cell-free medium exposed to TTFields showed little antitumor activity. These experiments separate the microglial effect both temporally and physically from the direct effects of TTFields on glioma cells. Human microglial conditioned medium also reduced proliferation in patient-derived GBOs, while co-implantation of pre-exposed microglia reduced early intracranial tumor burden. Previous work reported antitumor activity in conditioned medium from a TTFields-treated macrophage cell line[10]. Our study substantially extends this observation by demonstrating the effect in primary murine and human microglia, patient-derived organoids, and an intracranial setting. Together, these findings show that TTFields do not merely alter microglial markers during exposure; they induce a functional change that allows microglia to continue restraining glioma cells after the physical stimulus has been removed.

Our results also begin to explain how this microglial response is translated into tumor-cell injury. TTFields induced HIF-1α-associated glycolytic remodeling in microglia, and 2-DG treatment reduced the antitumor activity of conditioned medium collected thereafter, supporting a functional contribution of microglial glucose metabolism. In recipient glioma cells that had never been directly exposed to

TTFields, the resulting injury was characterized by altered glutathione metabolism, increased lipid oxidation and Fe^{2+} accumulation, disruption of antioxidant homeostasis, ferroptosis-compatible mitochondrial changes, and protection by ferroptosis-directed interventions. The agreement between transcriptomic, biochemical, ultrastructural, and pharmacological evidence supports ferroptosis-associated oxidative injury as an important downstream component of the microglial antitumor effect. These findings therefore connect metabolic remodeling in TTFields-exposed microglia with a defined form of stress in neighboring glioma cells. This cross-cellular mechanism provides a possible explanation for how the biological effects of TTFields can extend beyond directly exposed dividing cells and continue after treatment has ended. It also identifies microglial metabolic activity and glioma-cell susceptibility to ferroptosis as potential determinants of treatment response. Although the active soluble mediators remain to be identified, defining them should enable this pathway to be tested and therapeutically manipulated more precisely.

The experimental models used here were selected to address three related questions: whether microglia respond directly to TTFields, whether their antitumor activity persists after exposure, and how this activity is transmitted to glioma cells. Isolated-cell and conditioned-medium systems do not reproduce the full cellular and spatial complexity of human glioblastoma, but their reduced complexity was important for distinguishing direct microglial responses from secondary effects of TTFields-induced tumor-cell injury. Similarly, the co-implantation model was designed to test whether pre-exposed microglia retained biological activity in vivo, rather than to reproduce clinical TTFields treatment of an established tumor. The limited number of GBO models will require extension to larger patient cohorts, particularly to determine how the response varies across the molecular and cellular heterogeneity of glioblastoma. Nevertheless, the consistency of the central findings across single-cell analysis of patient-derived organoids, BV2 cells, primary murine and human microglia, multiple glioma models, field-free functional assays, and an intracranial setting supports their biological relevance. Taken together, our study identifies microglia as a direct and functionally important target of TTFields and links their metabolic remodeling to ferroptosis-associated injury in glioma cells. This work expands the current understanding of TTFields from a predominantly tumor-cell-directed treatment to a multicellular therapy whose effects are shaped by both malignant cells and the surrounding immune microenvironment.

Conclusion

This study identifies microglia as a direct and functionally relevant cellular target of TTF in glioblastoma. Using patient-derived glioblastoma organoids and complementary murine and human microglial models, we show that TTF induces coordinated immune, secretory, and metabolic remodeling in microglia and generates an antitumor effect that persists after field withdrawal. This response is associated with HIF-1α-related glycolytic remodeling, and inhibition of microglial glucose metabolism reduces the antitumor activity of the resulting conditioned medium. In neighboring glioma cells, the microglial secretome disrupts glutathione and lipid-redox homeostasis and promotes ferroptosis-associated oxidative injury. Together, these findings extend the biological effects of TTF beyond direct antimitotic activity and reveal a multicellular metabolic mechanism in which TTF reprograms microglial metabolism to influence

tumor-cell redox vulnerability. This framework provides a basis for further exploring microglial metabolism and tumor redox state as potential determinants of, and therapeutic targets for, TTF response in glioblastoma.

Abbreviations

2-DG
2-deoxy-D-glucose
CM
conditioned medium
GAM
glioma-associated microglia/macrophages
GBM
glioblastoma
GBO
glioblastoma organoid
GSH
reduced glutathione
GSSG
oxidized glutathione
HIF-1α
hypoxia-inducible factor 1 alpha
MHC-I
major histocompatibility complex class I
MHC-II
major histocompatibility complex class II
mTOR
mechanistic target of rapamycin
OVA
ovalbumin
PD-1
programmed cell death protein 1
PD-L1
programmed death-ligand 1
pMG
primary microglia
scRNA-seq
single-cell RNA sequencing
TME
tumor microenvironment

TTF
Tumor Treating Fields.

Declarations

Ethics approval and consent to participate

Fresh glioblastoma tissue was obtained from patients undergoing surgical resection in the Department of Neurosurgery, Huashan Hospital, Fudan University. Glioblastoma was diagnosed according to the 2021 WHO Classification of Tumours of the Central Nervous System. Written informed consent was obtained from all participants or their legal representatives. The study was approved by the Ethics Committee of Huashan Hospital, Fudan University (KY2024-1421) and was conducted in accordance with the Declaration of Helsinki.

All animal procedures were approved by the Animal Ethics Committee of Shanghai Medical College, Fudan University. Animal experiments were conducted and reported in accordance with the ARRIVE guidelines. C57BL/6 mice were obtained from GemPharmatech Co., Ltd. (Nanjing, China) and maintained under specific-pathogen-free conditions.

Availability of data and materials

The processed data supporting the findings of this study are provided within the article and its Supplementary Information. Raw sequencing data generated in this study are being deposited in a public repository, and the corresponding accession number(s) will be provided before publication. Additional data are available from the corresponding author upon reasonable request.

Competing interests

The authors declare that they have no competing interests.

Acknowledgement

This work was supported by the Shanghai Natural Science Foundation General Program (25ZR1401046) and the National Natural Science Foundation of China (82402440).

Authors’ contributions

Pengjie Hong: Conceptualization, Data curation, Formal analysis, Investigation, Methodology, Validation, Visualization, and Writing – original draft. Xianxin Qiu: Conceptualization and Funding acquisition. Wanzun Lin: Conceptualization, Formal analysis, Investigation, and Resources. Huiling Fang: Investigation. Zhengjin He: Conceptualization. Kezhu Chen, Tianwen Li, Junjie Zhong, and Tongming Zhu: Methodology. Qisheng Tang and Zhiguang Pan: Resources. Yang Wang: Conceptualization, Project administration, and Supervision. Hai Jiang: Conceptualization, Project administration, Supervision, and

Writing – review & editing. Dongxiao Zhuang: Conceptualization, Funding acquisition, Resources, Supervision, and Writing – review & editing. All authors read and approved the final manuscript.

References

1. Ostrom QT, Price M, Neff C, Cioffi G, Waite KA, Kruchko C, et al. CBTRUS Statistical Report: Primary Brain and Other Central Nervous System Tumors Diagnosed in the United States in 2015–2019. Neurooncology. 2022;24(Suppl 5):v1–95.
2. Weller M, Wick W, Aldape K, Brada M, Berger M, Pfister SM, et al. Glioma Nat reviews Disease primers. 2015;1(1):1–18.
3. Stupp R, Hegi ME, Mason WP, Van Den Bent MJ, Taphoorn MJ, Janzer RC, et al. Effects of radiotherapy with concomitant and adjuvant temozolomide versus radiotherapy alone on survival in glioblastoma in a randomised phase III study: 5-year analysis of the EORTC-NCIC trial. Lancet Oncol. 2009;10(5):459–66.
4. Brown CE, Alizadeh D, Starr R, Weng L, Wagner JR, Naranjo A, et al. Regression of Glioblastoma after Chimeric Antigen Receptor T-Cell Therapy. N Engl J Med. 2016;375(26):2561–9.
5. Cloughesy TF, Mochizuki AY, Orpilla JR, Hugo W, Lee AH, Davidson TB, et al. Neoadjuvant anti-PD-1 immunotherapy promotes a survival benefit with intratumoral and systemic immune responses in recurrent glioblastoma. Nat Med. 2019;25(3):477–86.
6. Desjardins A, Gromeier M, Herndon JE, Beaubier N, Bolognesi DP, Friedman AH, et al. Recurrent glioblastoma treated with recombinant poliovirus. N Engl J Med. 2018;379(2):150–61.
7. Hilf N, Kuttruff-Coqui S, Frenzel K, Bukur V, Stevanović S, Gouttefangeas C, et al. Actively personalized vaccination trial for newly diagnosed glioblastoma. Nature. 2019;565(7738):240–5.
8. Reardon DA, Brandes AA, Omuro A, Mulholland P, Lim M, Wick A, et al. Effect of Nivolumab vs Bevacizumab in Patients With Recurrent Glioblastoma: The CheckMate 143 Phase 3 Randomized Clinical Trial. JAMA Oncol. 2020;6(7):1003–10.
9. Bejarano L, Jordão MJC, Joyce JA. Therapeutic Targeting of the Tumor Microenvironment. Cancer Discov. 2021;11(4):933–59.
10. Klemm F, Maas RR, Bowman RL, Kornete M, Soukup K, Nassiri S, et al. Interrogation of the microenvironmental landscape in brain tumors reveals disease-specific alterations of immune cells. Cell. 2020;181(7):1643–60. e17.
11. Ginhoux F, Greter M, Leboeuf M, Nandi S, See P, Gokhan S, et al. Fate mapping analysis reveals that adult microglia derive from primitive macrophages. Science. 2010;330(6005):841–5.
12. Goldmann T, Wieghofer P, Jordão MJC, Prutek F, Hagemeyer N, Frenzel K, et al. Origin, fate and dynamics of macrophages at central nervous system interfaces. Nat Immunol. 2016;17(7):797–805.
13. Abels ER, Maas SLN, Nieland L, Wei Z, Cheah PS, Tai E, et al. Glioblastoma-Associated Microglia Reprogramming Is Mediated by Functional Transfer of Extracellular miR-21. Cell Rep.

2019;28(12):3105–e197.
14. Karimi E, Yu MW, Maritan SM, Perus LJM, Rezanejad M, Sorin M, et al. Single-cell spatial immune landscapes of primary and metastatic brain tumours. Nature. 2023;614(7948):555–63.
15. Khan F, Pang L, Dunterman M, Lesniak MS, Heimberger AB, Chen P. Macrophages and microglia in glioblastoma: heterogeneity, plasticity, and therapy. J Clin Investig. 2023;133(1).
16. Liu H, Sun Y, Zhang Q, Jin W, Gordon RE, Zhang Y et al. Pro-inflammatory and proliferative microglia drive progression of glioblastoma. Cell Rep. 2021;36(11).
17. Sarkar S, Döring A, Zemp FJ, Silva C, Lun X, Wang X, et al. Therapeutic activation of macrophages and microglia to suppress brain tumor-initiating cells. Nat Neurosci. 2014;17(1):46–55.
18. Gao X, Li S, Ding F, Liu X, Wu Y, Li J, et al. A Virus-Mimicking Nucleic Acid Nanogel Reprograms Microglia and Macrophages for Glioblastoma Therapy. Advanced materials (Deerfield Beach. Fla). 2021;33(9):e2006116.
19. Yeini E, Ofek P, Pozzi S, Albeck N, Ben-Shushan D, Tiram G, et al. P-selectin axis plays a key role in microglia immunophenotype and glioblastoma progression. Nat Commun. 2021;12(1):1912.
20. Stupp R, Taillibert S, Kanner A, Read W, Steinberg DM, Lhermitte B, et al. Effect of tumor-treating fields plus maintenance temozolomide vs maintenance temozolomide alone on survival in patients with glioblastoma: a randomized clinical trial. JAMA. 2017;318(23):2306–16.
21. Chen D, Le SB, Ghiaseddin AP, Manektalia H, Li M, O'Dell A et al. Efficacy and safety of adjuvant TTFields plus pembrolizumab and temozolomide in newly diagnosed glioblastoma: A phase 2 study. Med. 2025:100708.
22. Ballo MT, Conlon P, Lavy-Shahaf G, Kinzel A, Vymazal J, Rulseh AM. Association of Tumor Treating Fields (TTFields) therapy with survival in newly diagnosed glioblastoma: a systematic review and meta-analysis. J Neurooncol. 2023;164(1):1–9.
23. Kirson ED, Dbaly V, Tovarys F, Vymazal J, Soustiel JF, Itzhaki A, et al. Alternating electric fields arrest cell proliferation in animal tumor models and human brain tumors. Proc Natl Acad Sci USA. 2007;104(24):10152–7.
24. Kirson ED, Gurvich Z, Schneiderman R, Dekel E, Itzhaki A, Wasserman Y, et al. Disruption of cancer cell replication by alternating electric fields. Cancer Res. 2004;64(9):3288–95.
25. Gera N, Yang A, Holtzman TS, Lee SX, Wong ET, Swanson KD. Tumor treating fields perturb the localization of septins and cause aberrant mitotic exit. PLoS ONE. 2015;10(5):e0125269.
26. Giladi M, Schneiderman RS, Voloshin T, Porat Y, Munster M, Blat R, et al. Mitotic Spindle Disruption by Alternating Electric Fields Leads to Improper Chromosome Segregation and Mitotic Catastrophe in Cancer Cells. Sci Rep. 2015;5:18046.
27. Voloshin T, Kaynan N, Davidi S, Porat Y, Shteingauz A, Schneiderman RS, et al. Tumor-treating fields (TTFields) induce immunogenic cell death resulting in enhanced antitumor efficacy when combined with anti-PD-1 therapy. Cancer Immunol Immunother. 2020;69(7):1191–204.

28. Park J-I, Song K-H, Jung S-Y, Ahn J, Hwang S-G, Kim J, et al. Tumor-Treating Fields Induce RAW264.7 Macrophage Activation Via NK-kappaB/MAPK Signaling Pathways. Technol Cancer Res Treat. 2019;18:1533033819868225.
29. Kan T, Barsheshet Y, Haj Khalil T, Brant B, Voloshin T, Ben-Meir K et al. Pro-Inflammatory Macrophage Phenotype Skewing Induced by Tumor Treating Fields (TTFields). Int J Mol Sci. 2025;26(24).
30. Block ML, Zecca L, Hong J-S. Microglia-mediated neurotoxicity: uncovering the molecular mechanisms. Nat Rev Neurosci. 2007;8(1):57–69.
31. Orihuela R, McPherson CA, Harry GJ. Microglial M1/M2 polarization and metabolic states. Br J Pharmacol. 2016;173(4):649–65.
32. Saha D, Martuza RL, Rabkin SD. Macrophage polarization contributes to glioblastoma eradication by combination immunovirotherapy and immune checkpoint blockade. Cancer Cell. 2017;32(2):253–67. e5.
33. Pyonteck SM, Akkari L, Schuhmacher AJ, Bowman RL, Sevenich L, Quail DF, et al. CSF-1R inhibition alters macrophage polarization and blocks glioma progression. Nat Med. 2013;19(10):1264–72.
34. Zhai K, Huang Z, Huang Q, Tao W, Fang X, Zhang A, et al. Pharmacological inhibition of BACE1 suppresses glioblastoma growth by stimulating macrophage phagocytosis of tumor cells. Nat Cancer. 2021;2(11):1136–51.
35. Müller S, Kohanbash G, Liu SJ, Alvarado B, Carrera D, Bhaduri A, et al. Single-cell profiling of human gliomas reveals macrophage ontogeny as a basis for regional differences in macrophage activation in the tumor microenvironment. Genome Biol. 2017;18(1):234.
36. Park JI, Song KH, Jung SY, Ahn J, Hwang SG, Kim J, et al. Tumor-Treating Fields Induce RAW264.7 Macrophage Activation Via NK-κB/MAPK Signaling Pathways. Technol Cancer Res Treat. 2019;18:1533033819868225.

Figures

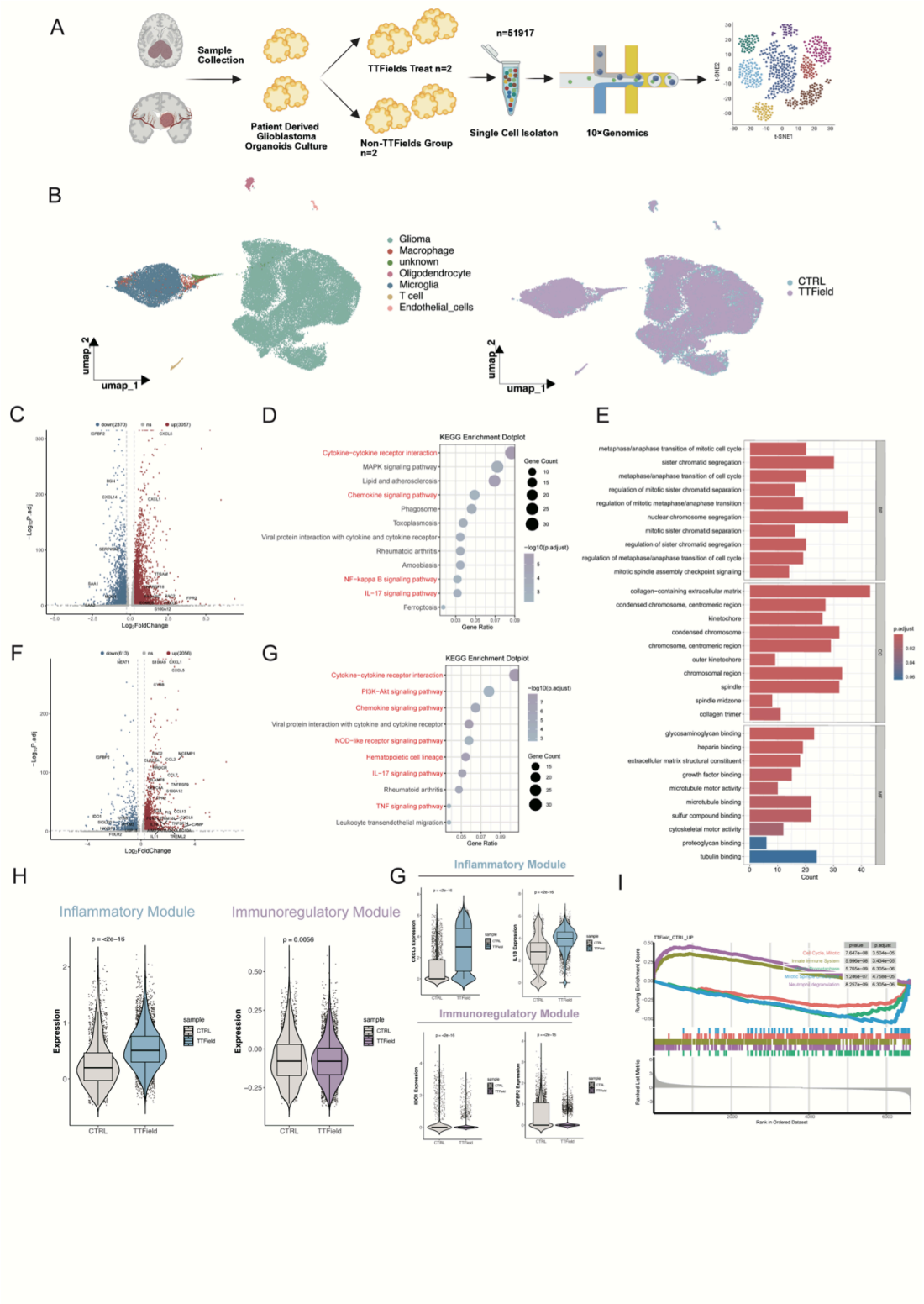


Figure 1

Single-cell transcriptomic profiling reveals coordinated glioma and microglial responses to TTFields in glioblastoma organoids.

(A) Schematic of the experimental workflow. Patient-derived glioblastoma organoids (GBOs) were analyzed under paired control and TTFields-treated conditions (1.4 V/cm for 40 h; n = 2 per condition),

followed by single-cell dissociation and 10x Genomics RNA sequencing. A total of 51,917 cells were retained for downstream analysis.

(B) UMAP visualization of all cells colored by annotated cell identity (left) or treatment condition (right). Major populations included glioma cells, microglia, macrophages, oligodendrocytes, T cells, endothelial cells, and an unclassified population.

(C) Volcano plot showing differentially expressed genes in glioma cells from TTFields-treated versus control GBOs. Red and blue indicate significantly upregulated and downregulated genes, respectively; gray indicates nonsignificant genes. A total of 3,057 genes were upregulated and 2,370 genes were downregulated following TTFields treatment.

(D) KEGG enrichment analysis of genes upregulated in TTFields-treated glioma cells. Dot size represents the number of genes assigned to each pathway, and color denotes −log10-adjusted P value.

(E) Gene Ontology enrichment analysis of genes downregulated in TTFields-treated glioma cells, grouped into biological process (BP), cellular component (CC), and molecular function (MF) categories. Bar length represents the number of enriched genes, and color indicates the adjusted P value.

(F) Volcano plot showing differentially expressed genes in microglia from TTFields-treated versus control GBOs. Red and blue indicate significantly upregulated and downregulated genes, respectively; gray indicates nonsignificant genes. A total of 2,056 genes were upregulated and 613 genes were downregulated following TTFields treatment.

(G) KEGG enrichment analysis of genes upregulated in TTFields-treated microglia. Dot size represents the number of genes assigned to each pathway, and color denotes −log10-adjusted P value.

(H) Violin and box plots showing inflammatory and anti-inflammatory/immunoregulatory module scores, together with the expression of representative inflammatory genes (*CXCL8* and *IL1B*) and immunoregulatory genes (*IDO1*and *IGFBP2*) in control and TTFields-treated microglia. Each dot represents an individual cell. Center lines indicate medians, boxes indicate interquartile ranges, and whiskers extend to 1.5 times the interquartile range. P values are shown in the plots.

(I) Gene set enrichment analysis of selected pathways in microglia from TTFields-treated versus control GBOs. Enrichment curves are plotted across the ranked gene list; positive enrichment scores indicate preferential enrichment in TTFields-treated microglia, whereas negative scores indicate enrichment in control microglia. Nominal and Benjamini–Hochberg-adjusted P values are shown.

Adjusted P values in differential-expression and enrichment analyses were calculated using the Benjamini–Hochberg method. BP, biological process; CC, cellular component; GBO, glioblastoma organoid; KEGG, Kyoto Encyclopedia of Genes and Genomes; MF, molecular function; TTFields, tumor treating fields.

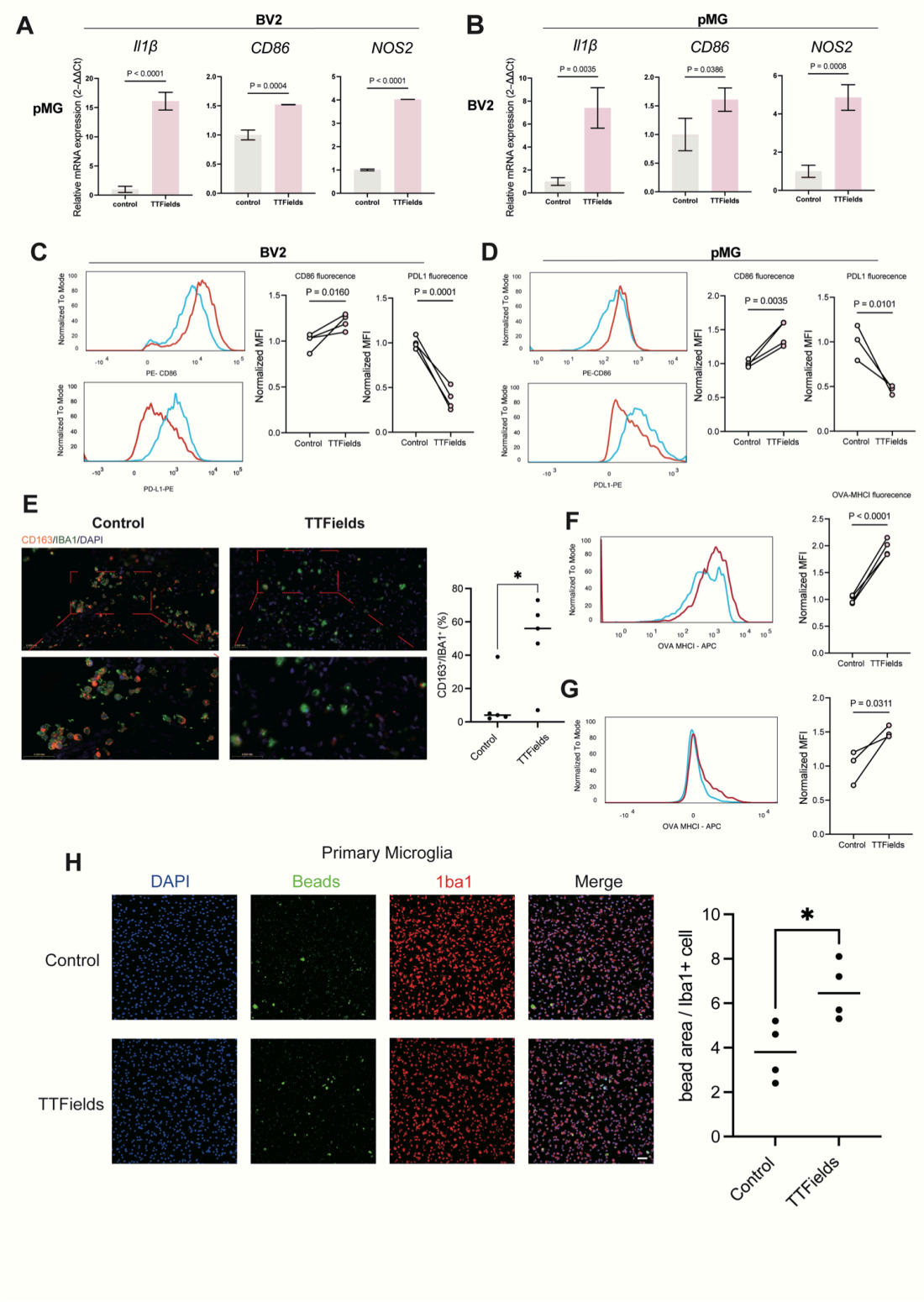


Figure 2

TTFields directly reprogram microglial phenotype and effector functions

(A, B)RT–qPCR analysis of *Il1b*, *Cd86*, and *Nos2* expression in BV2 cells **(A)** and primary microglia (pMG) **(B)** following TTFields treatment. Gene expression was normalized to the corresponding untreated control.

(C, D) Representative flow-cytometry histograms and quantification of normalized median fluorescence intensity (MFI) of CD86 and PD-L1 in BV2 cells **(C)**and pMG **(D)**. Connected points represent matched experiments performed with control and TTFields-treated cells.

(E) Representative immunofluorescence images of CD163 (red), IBA1 (green), and DAPI (blue) in control and TTFields-treated glioblastoma organoids (GBOs), together with quantification of the proportion of CD163-positive cells among IBA1-positive myeloid cells. Enlarged regions correspond to the areas indicated in the upper images.

(F, G) Representative flow-cytometry histograms and quantification of cell-surface OVA–MHC-I complexes following antigen exposure in BV2 cells **(F)** and pMG **(G)**. MFI values were normalized to the corresponding untreated controls.

(H) Representative fluorescence images and quantitative analysis of fluorescent-bead uptake by primary microglia. Nuclei were stained with DAPI (blue), microglia with IBA1 (red), and internalized fluorescent beads are shown in green. Phagocytic activity was quantified as bead-positive area normalized to the number of IBA1-positive cells.

Data are presented as mean ± SEM unless otherwise indicated. Each dot represents an independent biological replicate, and connected dots indicate paired measurements. Two-group comparisons were performed using two-tailed Student's *t*-tests, with paired *t*-tests used for matched experiments. Exact *P* values are shown where indicated; $P < 0.05$ was considered statistically significant.

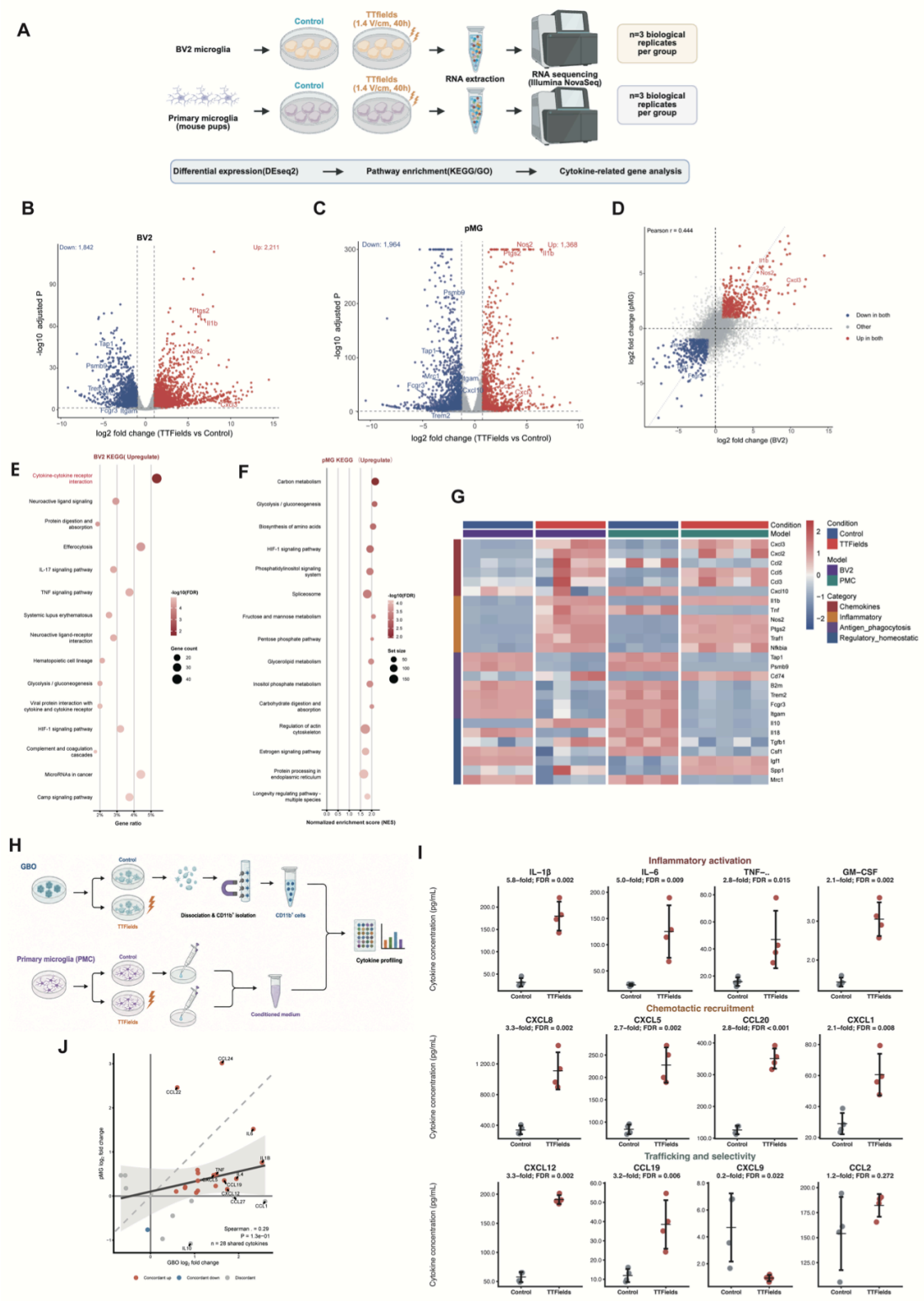


Figure 3

TTFields remodel microglial transcriptional and cytokine programs.

(A) Experimental workflow for bulk RNA sequencing of BV2 cells and primary mouse microglia (pMG). Cells were maintained under control conditions or exposed to TTFields at 1.4 V/cm for 40 h, followed by RNA extraction, Illumina NovaSeq sequencing, differential-expression analysis, pathway-enrichment

analysis, and focused analysis of cytokine-related genes. Three biological replicates were included per condition for each model.

(B) Volcano plot showing differential gene expression in TTFields-treated versus control BV2 cells. Genes increased and decreased following TTFields exposure are shown in red and blue, respectively, whereas genes not meeting the prespecified differential-expression criteria are shown in gray. Selected genes are labeled. A total of 2,211 genes were upregulated and 1,842 genes were downregulated.

(C) Volcano plot showing differential gene expression in TTFields-treated versus control pMG. Genes increased and decreased following TTFields exposure are shown in red and blue, respectively, whereas genes not meeting the prespecified differential-expression criteria are shown in gray. Selected genes are labeled. A total of 1,368 genes were upregulated and 1,964 genes were downregulated.

(D) Cross-model comparison of TTFields-induced gene-expression changes in BV2 cells and pMG. Genes increased or decreased in both models are shown in red and blue, respectively, whereas genes without concordant changes are shown in gray. The Pearson correlation coefficient is indicated.

(E) KEGG over-representation analysis of genes upregulated by TTFields in BV2 cells. Dot size represents the number of genes assigned to each pathway, and color represents −log10(FDR).

(F) KEGG gene-set enrichment analysis of pathways positively enriched in TTFields-treated pMG. Dot size represents gene-set size, and color represents −log10(FDR). The horizontal axis indicates the normalized enrichment score.

(G) Heatmap showing cytokine- and immune-related gene expression in control and TTFields-treated BV2 cells and pMG. Genes are organized into chemokine, inflammatory, antigen-processing/phagocytic, and regulatory/homeostatic modules. Values represent row-scaled expression z scores.

(H) Experimental workflow for cytokine profiling. GBOs were maintained under control conditions or exposed to TTFields, followed by dissociation and isolation of $CD11b^+$ myeloid cells. In parallel, conditioned medium was collected from control and TTFields-treated pMG. The resulting samples were subjected to multiplex cytokine profiling.

(I) Concentrations of representative cytokines measured in the $CD11b^+$ myeloid fraction isolated from control and TTFields-treated GBOs. Cytokines are organized into inflammatory activation, chemotactic recruitment, and trafficking/selectivity modules. Each dot represents one independent GBO sample (n = 4 per condition). Horizontal lines and error bars indicate mean ± SD. Fold changes and Benjamini–Hochberg-adjusted false-discovery rates (FDRs) are indicated above each analyte.

(J) Comparison of TTFields-induced cytokine changes between GBO-derived $CD11b^+$ myeloid samples and pMG conditioned medium for 28 cytokines measured in both systems. Red and blue points indicate cytokines concordantly increased or decreased, respectively, whereas gray points indicate cytokines with discordant changes. The dashed line denotes the line of identity. The solid line and shaded region

represent the fitted relationship and its 95% confidence interval. Spearman's correlation coefficient and P value are indicated.

RNA-sequencing differential-expression analysis was performed using DESeq2, with P values adjusted using the Benjamini–Hochberg method. Pathway-enrichment significance is reported as FDR. For cytokine profiling, statistical testing was performed on log2-transformed concentrations using two-sided Welch's t-tests followed by Benjamini–Hochberg correction across analytes.

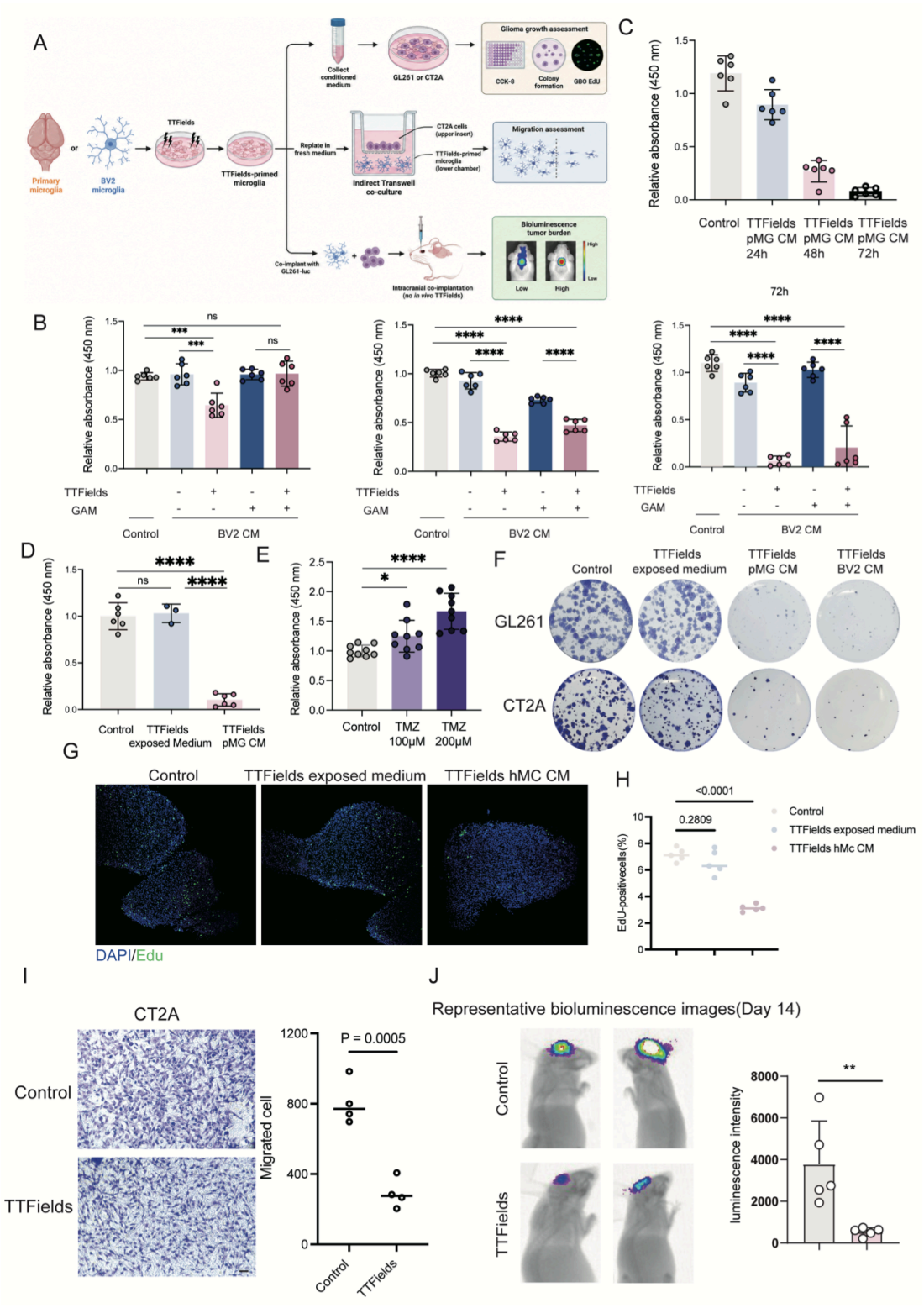


Figure 4

TTFields-primed microglia exert antitumor effects against glioma.

(A)Schematic of the experimental strategy for assessing the antitumor activity of TTFields-primed microglia.

(B)CCK-8 analysis of glioma-cell viability at 24, 48, and 72 h after exposure to CM from control or TTFields-primed BV2 cells. Where indicated, BV2 cells were preconditioned with GL261-derived CM to generate a GAM-like state before TTFields treatment.

(C)GL261 cell viability following exposure to CM from TTFields-primed primary microglia (pMGs) for 24, 48, or 72 h.

(D)GL261 cell viability after treatment with control medium, cell-free medium exposed to TTFields, or CM from TTFields-primed pMGs.

(E)GL261 cell viability following exposure to CM collected from control BV2 cells or BV2 cells treated with temozolomide (TMZ; 100 or 200 μM).

(F)Representative colony-formation assays in GL261 and CT2A cells treated with control medium, TTFields-exposed cell-free medium, TTFields-pMG-CM, or TTFields-BV2-CM.

(G)Representative EdU staining of glioblastoma organoids (GBOs) exposed to control medium, TTFields-exposed cell-free medium, or CM from TTFields-primed human microglial cells (hMCs). EdU, green; DAPI, blue. Scale bar:100μm.

(H)Quantification of EdU incorporation in GBOs under the indicated hMC-CM treatment conditions

(I)Representative Transwell images and quantification of CT2A migration in indirect co-culture with control or TTFields-primed microglia. Microglia were replated in the lower chamber with fresh medium after TTFields treatment, and CT2A cells were seeded in the upper inserts. Scale bar:100μm.

(J)Representative bioluminescence images and quantification of intracranial tumor burden on day 14 after orthotopic co-implantation of GL261-luc cells with untreated or TTFields-primed pMG cells.

Data are presented as mean ± SD. Each dot represents one biologically independent replicate or individual animal. Statistical significance was determined by [statistical tests]. *P* < 0.05, **P** < 0.01, ***P*** < 0.001, ****P**** < 0.0001; ns, not significant.

CM, conditioned medium; GAM, glioma-associated microglia/macrophage; GBO, glioblastoma organoid; hMC, human microglial cell; pMG, primary microglia; TMZ, temozolomide; TTFields, tumor treating fields.

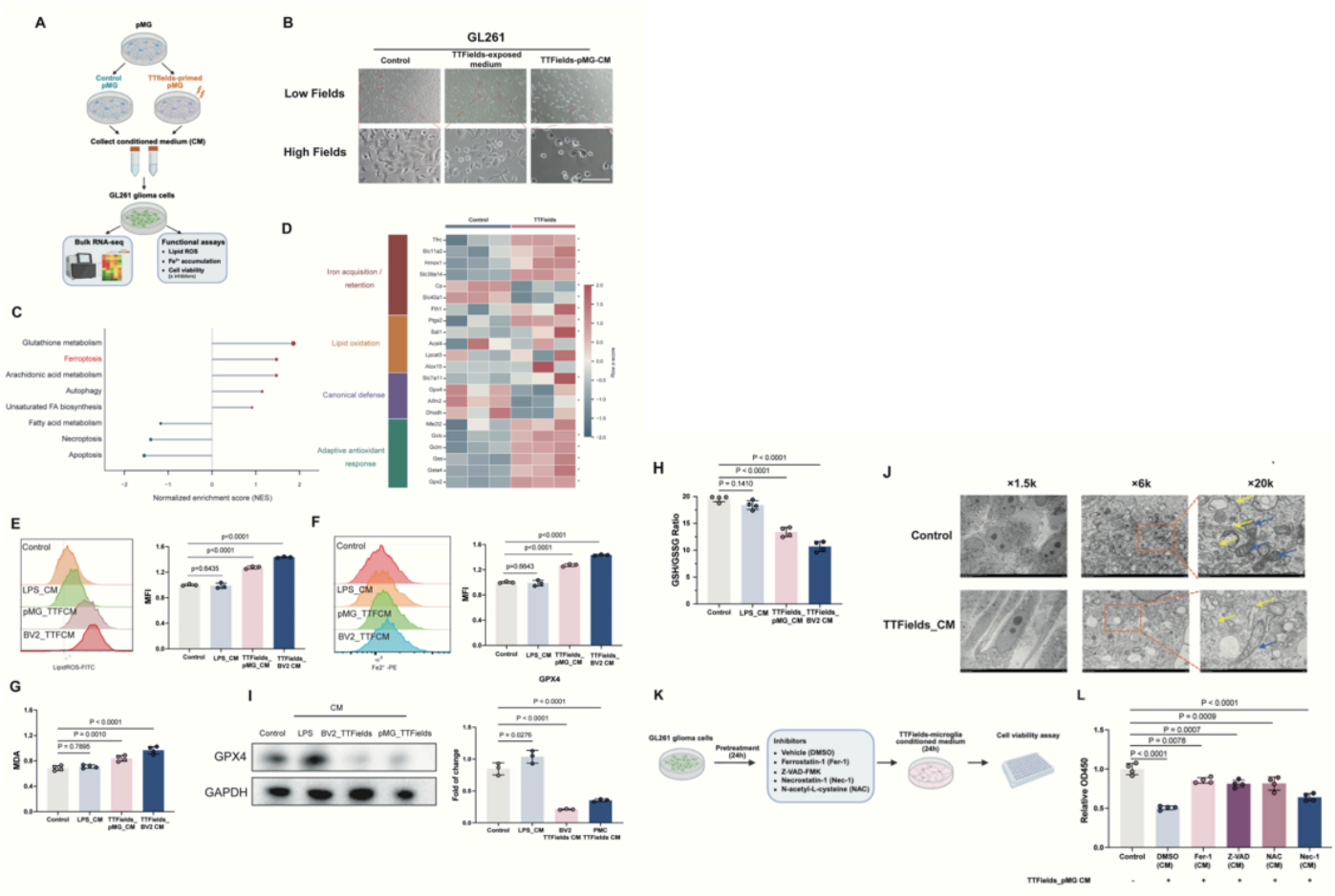


Figure 5

TTFields-primed microglial conditioned medium induces ferroptosis-associated oxidative stress in glioma cells.

(A) Schematic of conditioned-medium collection and subsequent analyses in GL261 cells.

(B) Representative phase-contrast images of GL261 cells following the indicated treatments. Scale bars:100μm.

(C) GSEA of selected cell-death and lipid-metabolism pathways in control and TTFields-pMG-CM-treated GL261 cells.

(D) Heatmap of genes involved in iron homeostasis, lipid oxidation, ferroptosis defense, and adaptive antioxidant responses.

(E and F) Representative flow-cytometry histograms and quantification of lipidROS (E) and intracellular Fe^{2+} (F) in GL261 cells following the indicated CM treatments.

(G and H) MDA levels (G) and GSH/GSSG ratios (H) in GL261 cells following the indicated treatments.

(I) Representative immunoblot and quantification of GPX4 expression in GL261 cells. GAPDH served as the loading control.

(J) Representative transmission electron microscopy images of GL261 cells treated with control or TTFields-pMG-CM. Blue arrows indicate mitochondria, whereas yellow arrows indicate endoplasmic reticulum cisternae.

(K) Schematic of the pharmacological rescue experiment using ferrostatin-1 (Fer-1), Z-VAD-FMK (Z-VAD), N-acetyl-L-cysteine (NAC), and necrostatin-1 (Nec-1).

(L) Relative viability of GL261 cells treated with TTFields-pMG-CM in the presence of the indicated inhibitors.

Data are presented as mean ± SD. Each dot represents one independent biological replicate; n =3-4. Statistical significance was determined by One-way ANOVA followed by Dunnett’s multiple-comparisons test. Exact P values are indicated in the figures. CM, conditioned medium; pMG, primary microglia.

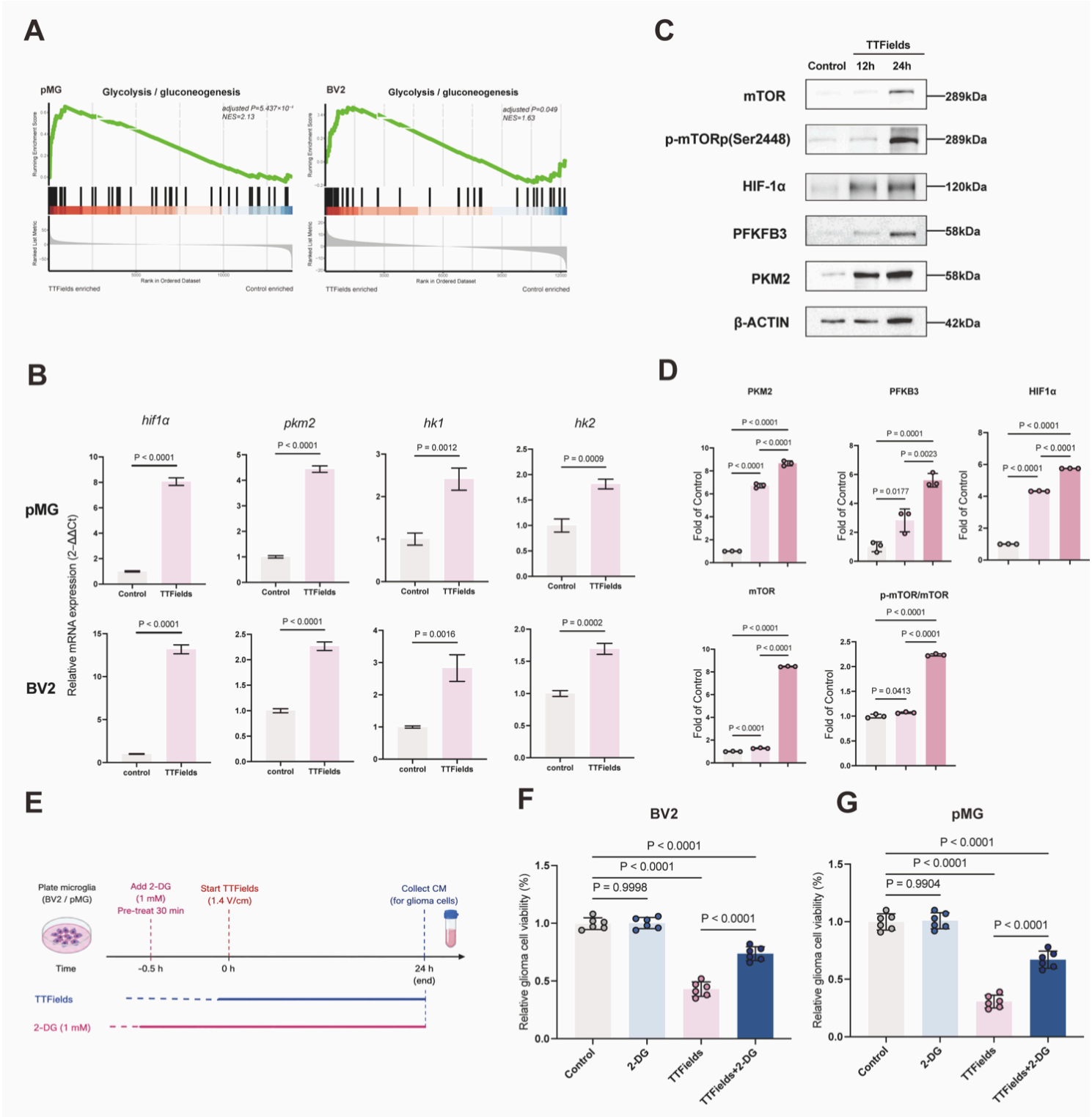


Figure 6

Glycolytic remodeling contributes to the antitumor activity of TTFields-primed microglia.

(A) Gene set enrichment analysis (GSEA) of the glycolysis/gluconeogenesis pathway in primary microglia (pMG) and BV2 cells following TTFields treatment. Normalized enrichment scores (NES) and adjusted *P*values are indicated.

(B) qRT–PCR analysis of *Hif1a*, *Pkm2*, *Hk1*, and *Hk2*expression in pMG and BV2 cells following TTFields

treatment. Gene expression was normalized to the indicated housekeeping gene and is presented relative to the corresponding control group.
(C) Representative immunoblots of mTOR, phospho-mTOR (Ser2448), HIF-1α, PFKFB3, and PKM2 in microglia under control conditions or after 12 or 24 h of TTFields exposure. β-ACTIN was used as a loading control.
(D) Quantification of PKM2, PFKFB3, HIF-1α, and mTOR protein abundance and the phospho-mTOR/mTOR ratio corresponding to the immunoblots in (C). Values are expressed relative to the control group.
(E) Schematic of the 2-deoxy-D-glucose (2-DG) rescue experiment. Microglia were pretreated with 1 mM 2-DG for 30 min before initiation of TTFields (1.4 V/cm), and 2-DG was maintained during TTFields exposure. Conditioned medium (CM) was collected after 24 h and transferred to glioma cells.
(F, G) Relative viability of glioma cells cultured with CM derived from control, 2-DG-treated, TTFields-treated, or TTFields plus 2-DG-treated BV2 cells **(F)** or pMG **(G)**. Glioma-cell viability was normalized to that of the corresponding control-CM group.

Data are presented as mean ± SD with individual biological replicates shown. For two-group comparisons, statistical significance was assessed using two-tailed unpaired Student's *t*-tests. For experiments containing control, 2-DG, TTFields, and TTFields + 2-DG conditions, data were analyzed by two-way ANOVA followed by Šídák's multiple-comparisons test for prespecified pairwise comparisons. Exact *P* values are shown where indicated.

Supplementary Files

This is a list of supplementary files associated with this preprint. Click to download.

- SupplementaryInformationmicroglia.docx
- supplementtable.xlsx
- westernoriginalgel.pdf